A new x-ray tomography method based on the 3d Radon transform compatible with anisotropic sources: supplemental material

M. Vassholz, B. Koberstein-Schwarz, A. Ruhlandt, M. Krenkel, and T. Salditt*
Institut für Röntgenphysik, Georg-August-Universität Göttingen, Friedrich-Hund-Platz 1, Göttingen, Germany

(Dated: December 9, 2015)

I. RADON TRANSFORM IN TWO AND THREE DIMENSIONS: BASIC DEFINITIONS, GEOMETRY AND NOTATION

The geometry of an x-ray projection image is depicted in Fig. 1. As sketched in (a), an x-ray passing through the object acquires line integrals of the observable $f(\underline{x})$, i.e. describing the attenuation, phase shift, scattering or fluorescence signal, and is recorded on the detector, aligned perpendicular to the direction of the beam $\underline{n}_\theta^\perp$. If the object is not scanned by a (focused) pencil beam, but illuminated by an extended and collimated parallel beam wavefront, the different paths through the object can be parameterized by the detector coordinate s, see (b). Conventional tomography based on the 2d Radon transform (2dRT) acquires a set of signal curves $g(\theta, s)$ for each projection angle θ between the beam direction and the object's coordinate system

$$g(\theta, s) := \int_{-\infty}^{\infty} f(s\underline{n}_\theta + r\underline{n}_\theta^\perp)\mathrm{d}r \ , \tag{1}$$

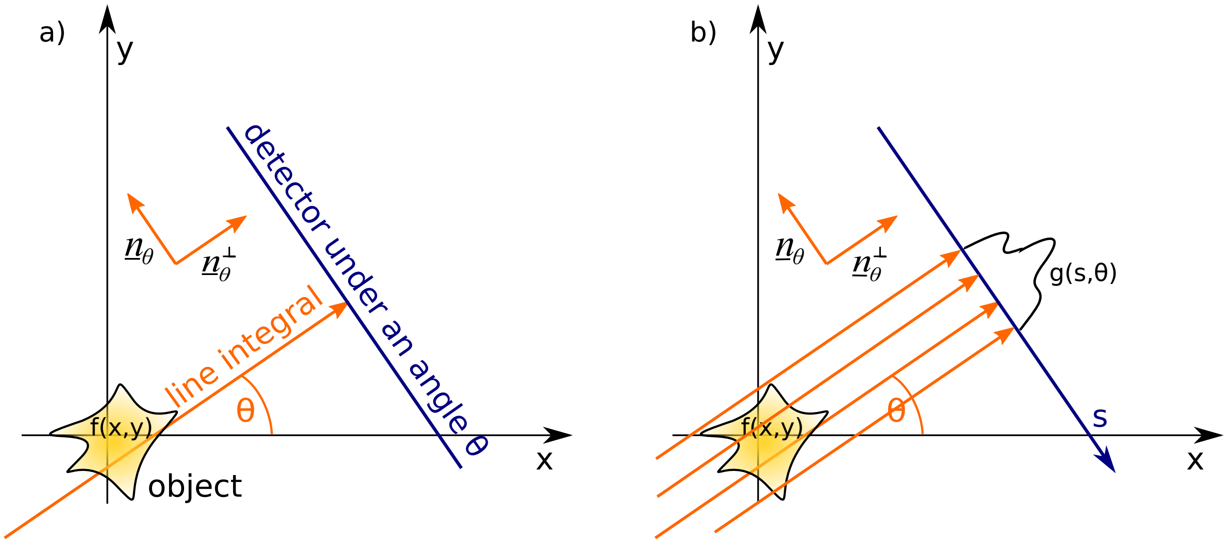

FIG. 1. Illustration of an x-ray projection image . (a) The signal recorded in a given detector pixel is given by the line integral along $\underline{n}_\theta^\perp$. (b) A conventional 2dRT tomographic scan records the function $g(s)$ for each rotation angle θ around the axis normal to the 2d reconstruction slice.

---

* tsaldit@gwdg.de

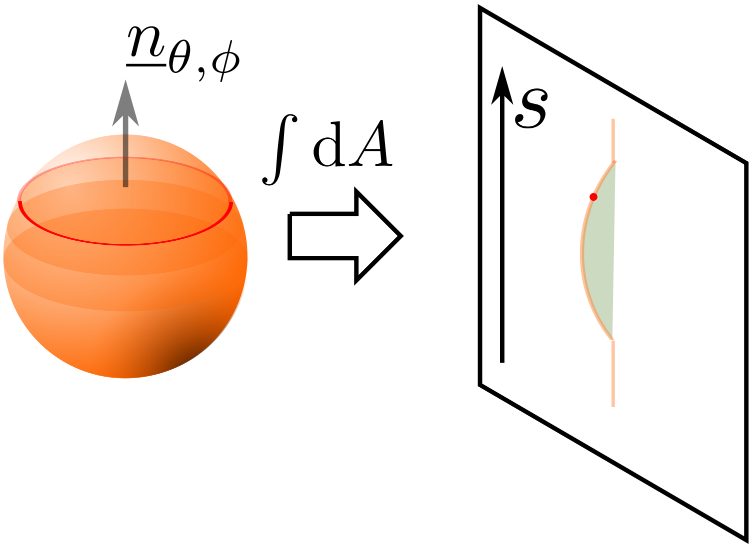

FIG. 2. Illustration of the 3d Radon transform. Every plane of the object becomes one point of the 3d Radon transform. For illustration one plane from the subspace $(\theta,\phi)^{\perp}$ and the corresponding point in the Radon transform is labeled red. s denotes the Radon coordinate.

where $\underline{n}_{\theta}^{\perp}$ is the unit vector along the projection line and $\underline{n}_{\theta}$ the unit vector perpendicular to this line, defining the 2d sinogram space $g(\theta,s)$. In conventional tomography, the 2dRT is used in a set of parallel planes through the object or body, i.e. also 3d reconstructions are obtained from a set of 2dRTs. Contrarily, the 3d Radon transform (3dRT) of a function $f(\underline{x})$, $\underline{x} \in \mathbb{R}^3$ requires integrals over planes according to

$$(\mathcal{R}f)(\underline{n}_{\theta,\phi},s) := \int_{\underline{y}\in(\theta,\phi)^{\perp}} f(s\,\underline{n}_{\theta,\phi}+\underline{y})\,\mathrm{d}^2y = \int \mathrm{d}^3x\, f(\underline{x})\,\delta(\underline{x}\cdot\underline{n}_{\theta,\phi}-s)\ , \tag{2}$$

where $(\theta,\phi)^{\perp}$ is the subspace of $\mathbb{R}^3$ perpendicular to $\underline{n}_{\theta,\phi}$. For a given point $\underline{n}_{\theta,\phi}$ on the unit sphere, a parallel set of planes intersects the object, each plane contributing a measurement point by two-dimensional integration of the object function over that plane, see Fig. 2. While the generation of a complete 2dRT data set only requires rotation around one axis, the 3dRT requires a rotation over two angles, for example parameterized by θ and ϕ, to cover the entire unit sphere, or equivalently to obtain sets of planes intersecting the object at all possible angles. Not withstanding more complex realizations of area integrals, such as approximated by data obtained with extended sources, there is a simple way of constructing data for 3dRT from the 2d projection, by post-processing of the projection images. Namely, the projection images must be integrated along one direction, yielding a one-dimensional profiles corresponding to the area as required for the 3dRT, see Fig. 3. We denote this procedure as 'post-integration'.

II. FOURIER SLICE THEOREM AND REPRESENTATION OF DATA RECORDED BY THE 2DRT AND THE 3DRT

The Fourier Slice Theorem (FST) is often invoked in tomography, if not as a starting point for reconstruction, at least to better understand the structure of the recorded data. Here we briefly compare the structure of 3dRT and

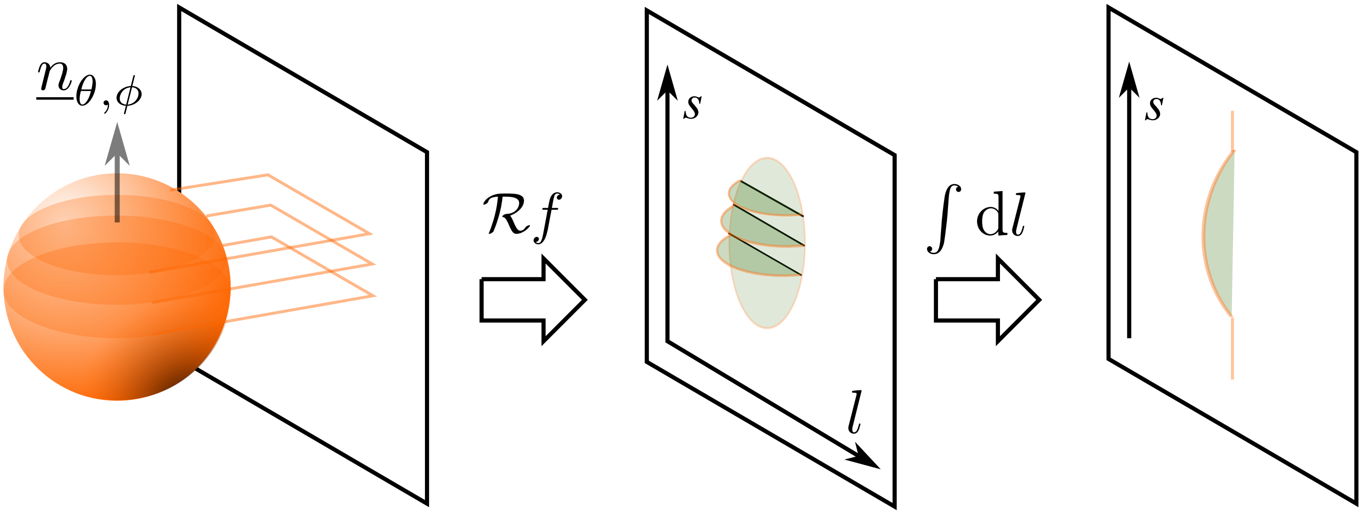

FIG. 3. Relation between the 2dRT and 3dRT. The conventional projection image is formed by the integral through the object along the direction perpendicular to the detector.By integrating along a direction parallel to the detector (here denoted by coordinate l), an integral over one plane through the object is performed, and hence the prerequisite for the 3d Radon transform. The present work is motivated by the idea that such an integral can be approximately also computed from projections recorded with sources which are extended in the direction of l, over which the data is integrated out.

.

2dRT data with help of the FST. In arbitrary dimension n, the FST specifies the relationship between the Fourier transform of the entire object data and the 1d Fourier transform of the orthogonal space to its $(n-1)$-dimensional hyperplanes, according to

$$\begin{aligned}
(\mathcal{F}_s(\mathcal{R}f))\,(t) &= \frac{1}{\sqrt{2\pi}}\int_{\mathbb{R}} (\mathcal{R}f)(\underline{n}_\theta, s)\ \mathrm{e}^{-ist}\mathrm{d}s && (3)\\
&= \frac{1}{\sqrt{2\pi}}\int_{\mathbb{R}} \mathrm{d}s\ \mathrm{e}^{-ist}\int_{\underline{y}\in\theta^\perp} f(\underbrace{s\,\underline{n}_\theta + \underline{y}}_{\underline{x}\in\mathbb{R}^n})\mathrm{d}^{n-1}y && (4)\\
&= \frac{1}{\sqrt{2\pi}}\int_{\mathbb{R}^n} \mathrm{d}^n x\ \mathrm{e}^{-i(\overbrace{\underline{x}\cdot\underline{n}_\theta}^{s})t}\, f(\underline{x}) && (5)\\
&= (2\pi)^{\frac{n-1}{2}}(\mathcal{F}f)(\underline{n}_\theta\cdot t). && (6)
\end{aligned}$$

The Fourier transform of $(\mathcal{R}f)$ with respect to s, denoted with $\mathcal{F}_s$, is hence always a line in the direction of $\underline{n}_\theta$ in Fourier space of $(\mathcal{F}f)$. With full knowledge of $(\mathcal{R}f)$ it is therefore possible to reconstruct the Fourier transform $(\mathcal{F}f)$, and hence also by Fourier back transformation the original function f, according to

$$\begin{aligned}
f(\underline{x}) &= (\mathcal{F}^{-1}(\mathcal{F}f))(\underline{x}) && (7)\\
&= (2\pi)^{-\frac{n-1}{2}}(\mathcal{F}(\mathcal{F}_s(\mathcal{R}f)))(\underline{x}) && (8)\\
&= (2\pi)^{-n+\frac{1}{2}}\int_{\mathbb{R}^n}\mathrm{d}^n k\ \mathrm{e}^{i\underline{k}\cdot\underline{x}}\left(\mathcal{F}_s(\mathcal{R}f)\left(\frac{\underline{k}}{|\underline{k}|}, s\right)\right)(|\underline{k}|) && (9)\\
&= (2\pi)^{-n+\frac{1}{2}}\int_{\mathbb{R}}\mathrm{d}t\, t^{n-1}\int_{S^{n-1}}\mathrm{d}\underline{n}_\theta\ \mathrm{e}^{i\underline{x}\cdot\underline{n}_\theta t}\left(\mathcal{F}_s(\mathcal{R}f)(\underline{n}_\theta, s)\right)(t)\ , && (10)
\end{aligned}$$

where the boundary of the n-dimensional unit ball is denoted with S^{n-1}. Reconstruction via the FST is conceptionally simple, but often hampered by regridding and interpolation artifacts, since the digital Fourier transform at least in the

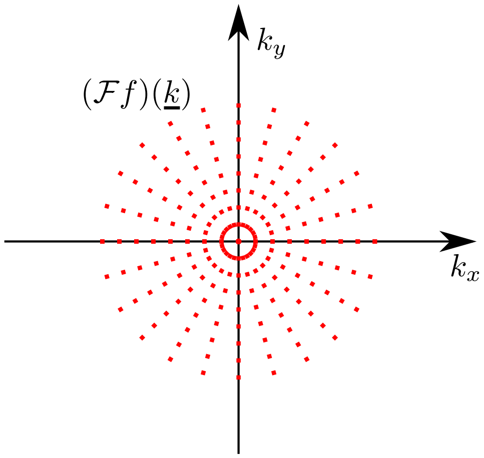

FIG. 4. Data points in Fourier space do not lay on a Cartesian grid, but are equally distanced in polar coordinates. For back transformation to real space, the data first has to be interpolated from polar to Cartesian coordinates.

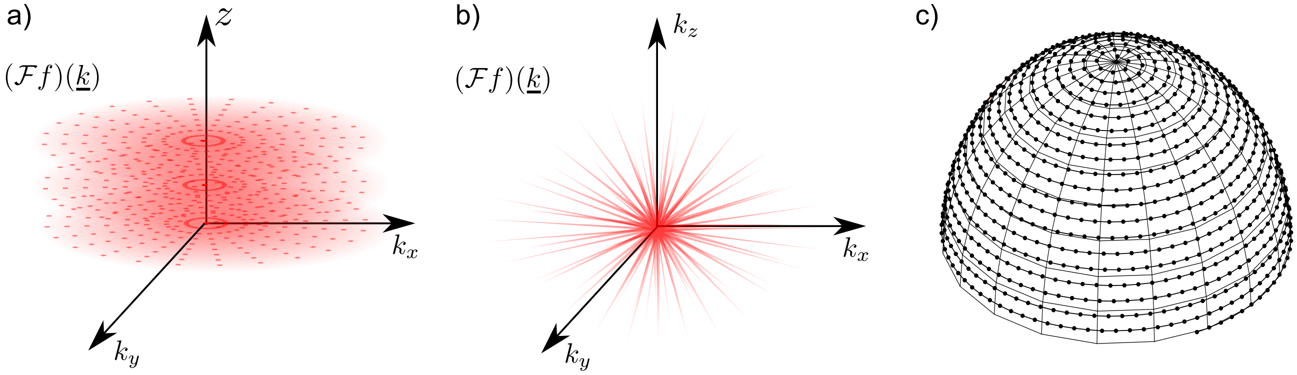

FIG. 5. (a) Stack of 2d Fourier planes with the real space coordinate along the z-axis. (b) Fourier slice theorem in three dimensions. The Fourier transformed Radon Transform generates a "hedgehog-like" structure with data spikes in 3d Fourier space, corresponding to all points on the unit sphere θ, ϕ, where data has been recorded. (c) N sampling points equally distributed on the upper half sphere.

standard implementations requires data on a Cartesian grid, while the recorded data is acquired on lines intersecting at zero, see Fig. 4. For conventional tomography of 3d objects, the object is divided into a set of parallel 2d planes and the reconstruction is performed separately for each of these planes. Instead of the 3d Fourier space of the entire object, one works in a hybrid space consisting of a stack of 2d Fourier planes, where the coordinate along the height of stack is still a real space coordinate, see the comparison between the Fourier representation of 2dRT and 3dRT in Fig. 5.

III. INVERSION FORMULA FOR THE 3DRT

Due to the mentioned regridding artifacts, tomographic reconstruction is in most cases not carried out based on the FST, even if recent progress has led to a raised interest in the Fourier based reconstruction methods [1]. Instead, filtered back projection is the method of choice for all but a few applications. How do back projection methods, which are conventionally performed in the 2dRT context, extend to the 3dRT? To this end, it is helpful to consider a general reconstruction formula valid for any dimension n, and for different sequences of filtering and back projection operators. For such a general inversion formula [2, 3], two additional operator definitions are needed, first the back projection operator $\mathcal{R}^{\#}$ defined by

$$\left(\mathcal{R}^{\#} g\right)(\underline{x}) := \int_{S^{n-1}} \mathrm{d}\underline{n}_\theta \, g(\underline{n}_\theta, \underline{x} \cdot \underline{n}_\theta), \tag{11}$$

where the integral is over the unit vector $\underline{n}_\theta$ covering the unit sphere in n dimensions. For the special case of 3d we also use the notation $\underline{n}_{\theta,\phi}$ to explicitly stress the two angles of spherical coordinates. Note that $\mathcal{R}^{\#}$ is the dual not the inverse operator to the operator $\mathcal{R}$ of the forward problem. Second, and in view of the required filtering steps, the Riesz operator I (also denoted as Riesz potential) is needed, as defined in n dimension [2]

$$\mathcal{F}(I^\alpha f)(\underline{k}) = |\underline{k}|^{-\alpha} (\mathcal{F} f)(\underline{k}), \tag{12}$$

by its action on a function $f(\underline{x})$ $\mathbb{R}^n \to \mathbb{R}$, for selectable parameter $\alpha < n$. Assuming $(\mathcal{F} f)$ at $\underline{k}$ to be sufficiently smooth and the inverse Fourier transform well defined, we have

$$(I^\alpha f)(\underline{x}) = \mathcal{F}^{-1}\left(|\underline{k}|^{-\alpha} (\mathcal{F} f)(\underline{k})\right), \tag{13}$$

and hence the inverse of the operator I^α is $I^{-\alpha}$ with

$$\begin{aligned} (I^\alpha I^{-\alpha} f)(\underline{x}) &= \mathcal{F}^{-1}\left(|\underline{k}|^{\alpha} |\underline{k}|^{-\alpha} (\mathcal{F} f)(\underline{k})\right) && (14) \\ &= f(\underline{x}). && (15) \end{aligned}$$

With these operator definitions, a general inversion formula can be derived [3] to reconstruct f from $\mathcal{R} f$,

$$f(\underline{x}) = \frac{1}{2} (2\pi)^{-n+1} \left(I^{-\alpha} \mathcal{R}^{\#} I^{\alpha+1-n} \mathcal{R} f\right)(\underline{x}) \ . \tag{16}$$

Since the parameter $\alpha < n$ can be freely selected, we get in fact a family of possible reconstruction formulas. While yielding the same reconstruction for ideal data, the different choices of α can behave very differently, however, for noisy or inconsistent data. Two cases are particularly noteworthy, firstly the so-called *filtered layergram* reconstruction obtained for $\alpha = n - 1$ and with $I^0 = 1$, leading to

$$\begin{aligned} f(\underline{x}) &= \frac{1}{2} (2\pi)^{-n+1} \left(I^{n-1} \mathcal{R}^{\#} \mathcal{R} f\right)(\underline{x}) && (17) \\ \Leftrightarrow (\mathcal{F} f)(\underline{k}) &= \frac{1}{2} (2\pi)^{-n+1} |\underline{k}|^{n-1} \left(\mathcal{F}(\mathcal{R}^{\#} \mathcal{R} f)\right)(\underline{k}) \ . && (18) \end{aligned}$$

This method consists of four steps: first back projection of the (unfiltered) data by the operator $\mathcal{R}^{\#}$, then the 3d Fourier transform, followed by a Fourier filtering step by multiplication with $|\underline{k}|^{n-1}$, and finally inverse Fourier transform. For n odd, I^{-n+1} is essentially a differential operator $I^{-n+1} = (-\Delta)^{(n-1)/2}$, and for $n = 3$ in particular reconstruction can be written in terms of the Laplace operator Δ as

$$f(\underline{x}) = \frac{1}{2} (2\pi)^{-n+1} \left(\Delta \mathcal{R}^{\#} \mathcal{R} f\right)(\underline{x}). \tag{19}$$

Although the reconstruction by filtered layergram is conceptionally quite simple and can be implemented in a straightforward manner, its 2d version is not used since it proved not to be robust with respect to noise and other imperfections in data acquisition. Instead, one prefers back projection of the filtered signal, i.e. the so-called *filtered back projection* scheme, obtained for $\alpha = 0$

$$f(\underline{x}) = \frac{1}{2}(2\pi)^{-n+1}\left(\mathcal{R}^{\#} I^{1-n}\mathcal{R}f\right)(\underline{x}) \qquad \text{with} \tag{20}$$

$$\left(\mathcal{F}(I^{1-n}g)\right)(t) = |t|^{n-1}(\mathcal{F}g)(t) \qquad . \tag{21}$$

The modulus in the filtering term $|t|^{n-1}$ has interesting consequences regarding the dimensionality of reconstruction. The fact that for even dimensions (such as the conventional $n = 2$), $n-1$ is odd so that $|t|^{n-1} = t^{n-1}\cdot\mathrm{sgn}(t)$, while for uneven n, $|t|^{n-1} = t^{n-1}$ entails a completely different structure of the problem. In fact, the explicit reconstruction formulas derived from (21) for the two cases are quite different. [3]. For n even, one obtains

$$f(\underline{x}) = \frac{i}{2\pi}(2\pi)^{-n+1}(-i)^{n-1}\int_{S^{n-1}} \mathrm{d}\underline{n}_\theta \int_{\mathbb{R}} \frac{\mathrm{d}z}{s-z}\left(\frac{\partial}{\partial z}\right)^{n-1}(\mathcal{R}f)(\underline{n}_\theta, z)\bigg|_{s=\underline{x}\underline{n}_\theta} , \tag{22}$$

with the Hilbert transform $\mathcal{H}(u)(t) = \frac{1}{\pi}\int\frac{\mathrm{d}z u(z)}{t-z}$. Contrarily, for n odd, the following reconstruction formula can be derived

$$f(\underline{x}) = \frac{i^{n-1}}{2}(2\pi)^{-n+1}\left(\mathcal{R}^{\#}\left(\frac{\partial}{\partial s}\right)^{n-1}(\mathcal{R}f)(\underline{n}_\theta, s)\right)(\underline{x}). \tag{23}$$

Important consequences can be inferred from the differences in these two reconstruction formulas. For odd dimensions n, the Radon transformation has local properties. For reconstruction of $f(\underline{x})$ at the position $\underline{x}$, only the Radon transform $(\mathcal{R}f)(s, \underline{n}_\theta)$ and its second derivative at positions $s = \underline{x}\underline{n}_\theta$ enters, in contrast to even n, where reconstruction at a given point is influenced by non-local object structure via the Hilbert integral transform. This important difference gives an entirely different motivation to using the 3dRT, in addition to the main motivation (relaxed source condition) put forward in this work. The different strategies for reconstruction in the framework of the 3dRT as briefly sketched here, are illustrated in Fig.6.

IV. ANGULAR SAMPLING

We have seen in Fig. 5(b) what the sampling of the Fourier domain looks like for a discrete angular sampling of the 3dRT. According to the FST we get a data spoke in Fourier space for each direction of $\underline{n}_{\theta,\phi}$. We now want to show how we have to sample $\underline{n}_{\theta,\phi}$ for N_p directions, to get an equal distribution of data spokes in Fourier space.

While it is trivial to distribute N_p angles equally in the interval $[0, \pi[$ for the 2dRT, it is not that obvious for the 3dRT case, as $\underline{n}_{\theta,\phi}$ is distributed over the entire surface of the 3d unit sphere S^2. The problem can be formulated by distributing N_p points equally on the surface of the unit sphere, which is a well-known problem in mathematics. There is no analytical solution to this problem if the number of points N_p is large. However, a variety of numerical solutions are proposed in the literature [4]. In this work the algorithm described in [5] is used to distribute N_p points equally along a spiral on the unit sphere. For symmetry reasons, it is sufficient to sample only one hemisphere, hence the algorithm will be used to distribute $2N_p$ positions on the unit sphere, whereas only N_p positions of one hemisphere are used for the measurements, as shown in Fig. 5(c). The angles (θ, ϕ) correspond to the angles of spherical coordinates for the sampling points.

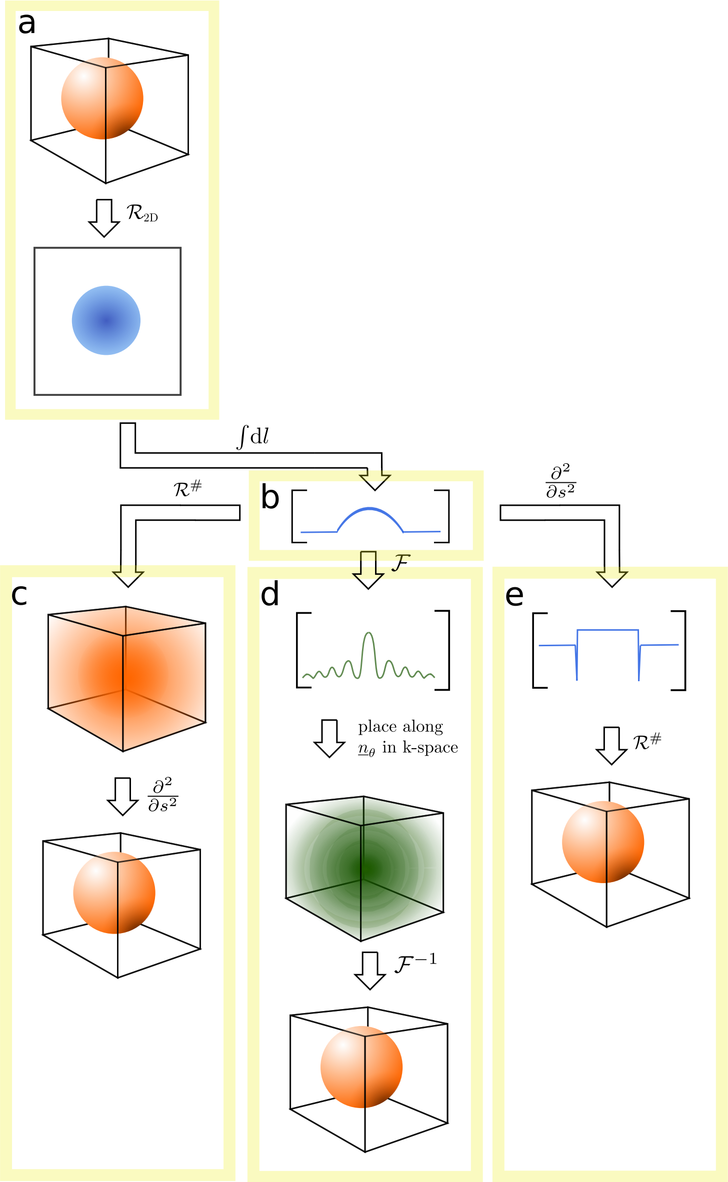

FIG. 6. Different ways of reconstructing an object within the 3dRT framework: (**a**) The object, as illustrated here for the case a sphere, is first projected on to the detector, similar to a single projection image of a 2dRT data set. (**b**) By integrating over l the 3dRT is generated. Alternatively, the 3d Radon transform can be generated directly by integration over a plane of the object. (**c**-**e**) illustrate the different reconstruction methods: (**c**) filtered layergram, (**d**) Fourier slice theorem, (**e**) back projection inversion formula. Orange color represents the real space, blue color the Radon space and green color the Fourier space.

V. EXPERIMENT: DETAILS OF THE SETUPS AND DATA ACQUISITION

A summary of the experimental parameters is given in Table I.

Hazel nut data set: A standard sealed tube x-ray source (DX-Mo10x1-P, GE-Seifert, Germany) with Molybdenum target and source size of 10 mm × 1 mm was used at a power of 45 kV × 45 mA. The beam was extracted under a take-off angle of 6° yielding an effective source size of 1 mm × 1 mm. A fully motorized high-precision slit system (type: 3014.4, Huber Diffraktionstechnik, Germany) with tungsten blades positioned at 10 cm behind the anode was used to define the beam. Anisotropic conditions were set by choosing the gap to 5 mm × 0.1 mm (h×v). After passing an evacuated flight tube, the beam illuminated the sample at $z_{01} = 173\,\mathrm{cm}$, placed on a κ-type diffractometer (type: 515.200, Huber Diffraktionstechnik, Germany), equipped with a fully motorized xyz-table. Projection images were recorded with a pixelated detector (Timepix Hexa H05-W0154, X-ray Imaging Europe, Germany) positioned at $z_{12} = 80.7\,\mathrm{cm}$ behind the sample with a pixel size of 55 µm and 500 µm thick silicon sensor material. The 3dRT scan with $\theta \in [0, \pi/2]$ and $\phi \in [0, 2\pi]$ was implemented with 4.5 s acquisition time for each of the 8001 projections. Raw data correction implied a mask for bad pixels and a division by the empty beam profile.

Match data set: A high-brilliance liquid-metal-jet x-ray source (JXS-D2-001, Excillum, Sweden) was used [8] with a Galinstan (GaInSn alloy) liquid-metal-jet anode providing roughly 10-times higher brilliance as conventional micro-CT sources. The characteristic K_α line of Ga with 9.25 keV photon energy was used for the present experiment. The source was operated at 70 kV and 60 W e-beam power. The e-beam spot size was set to 5 µm × 100 µm (h×v FWHM) , i.e. the source was deliberately enlarged in the vertical direction to emulate the anisotropic case. The sample was mounted at $z_{01} = 22.5\,\mathrm{cm}$ on a self-made goniometer consisting of two piezo-rotary positioners. A fiber-coupled scintillator-based detector with a custom scintillator (15 µm GdOS:Tb, Photonic Science) and a sCMOS-Chip with 6.54 µm pixel size (2048×2048 pixels, Photonic Science) was used. Raw data correction implied a mask for bad pixels, a correction by the dark field of the sCMOS and a division by the empty-beam profile.

VI. RECONSTRUCTION: DETAIL OF THE NUMERICAL IMPLEMENTATION

To obtain 3dRT data from the set of x-ray projection images for different pair of angles (θ, ϕ), a numerical 2dRT is performed on each of the projection images within an angular range of $\Delta\theta$ around the direction of high resolution for a discrete set of angles $\theta' \in [-\Delta\theta/2, \Delta\theta/2]$, yielding a number of δN 1d projection profiles $g_{\theta+\theta',\phi}(s)$ for each x-ray projection image, as shown in Fig. 7(a). Each 1d projection profile corresponds to a central slice in the 2d Fourier space of the x-ray projection image (cf. Fig. 7(b)). The angular range $\Delta\theta$ has to be chosen carefully depending on the anisotropy of the source, such that the central slices cover mainly high resolution information in Fourier space.

The 3d volume structure of the sample is reconstructed using the FBP. This is done in three steps: (i) Filtering: The second derivative with respect to the Radon coordinate s of each 1d projection profile is obtained by multiplication with the squared Fourier coordinate k^2 in the 1d Fourier domain. (ii) Each filtered 1d projection profile for the same angle ϕ is back projected in 2d by its corresponding angle θ using standard 2d back projection routines, yielding a set of back projected 2d images $G_\phi(x, y)$ for different angles ϕ. (iii) Each 2d image $G_\phi(x, y)$ is back projected to 3d space slice by slice, using standard 2d back projection routines, as known from conventional 2dRT-based tomography.

For the hazel nut data set a number of $\delta N = 81$ 1d projection profiles per x-ray projection within an angular range of $\Delta\theta = 20°$ was used for the reconstruction. For the reconstruction of the match data set the respective values are $\delta N = 161$ and $\Delta\theta = 20°$.

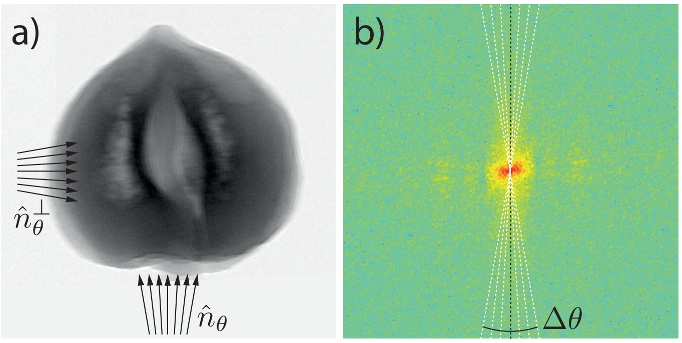

FIG. 7. 3dRT data generation for moderately elongated source spots: Instead of taking only one central slice along the high resolution direction (indicated by the black dashed line) of the Fourier domain (b) for each projection by adding up each projection along one direction, central slices for different angles θ within a certain range $\Delta\theta$ around the high resolution direction are taken, as indicated by the white dashed lines in (b). This is carried out by adding up the x-ray projections along a set of directions $\underline{n}_\theta^\perp$ in real space (a), i. e. by performing a 2dRT for a set of angles within the range $\Delta\theta$ for each projection.

Data Set	Hazel Nut	Match
source type	Mo target sealed tube	Galinstan liquid metal jet
effective source size (h×v)	1 mm × 0.1 mm	5 µm × 100 µm
counting time [s]	4.5	3
pixel size in detection plane [µm]	55	6.54
pixel size in object plane [µm]	37.5	3.1
distance source to sample z_{01} [cm]	173	22.5
distance sample to detector z_{12} [cm]	80.7	24.8
number of x-ray projections N_p	8001	10011
reconstructed volume size [voxel]	450^3	1800^3
number of numerical 2dRT per x-ray projection δN	81	161

TABLE I. Parameters of the experimental setups.

VII. PHASE CONTRAST: SIMULATIONS

3dRT-based tomography provides a direct reconstruction scheme for phase retrieval of pure phase objects. A. V. Bronnikov used this relation in 1999 to derive a phase retrieval scheme for 2dRT-based tomography [9, 10].

Consider a monochromatic coherent wave field with wavelength λ illuminating a pure phase object with refractive decrement $\delta(\underline{x})$ and hence a phase shift of $\varphi = 2\pi\,\delta/\lambda$. In an x-ray experiment the 2d intensity distribution $I_\phi^d(x,y)$ in an observation plane behind the object at a distance $z = d$ is measured for each projection angle ϕ. If the incoming intensity distribution $I^0(x,y)$ is known, one can calculate the deviation of the normalized intensity from unity, defined as

$$\bar{g}_\phi(x,y) := \frac{I_\phi^d(x,y)}{I^0(x,y)} - 1. \tag{24}$$

The quantity $\bar{g}_\phi(x,y)$ is related to the projected phase shift of the sample $\bar{\varphi}_\phi(x,y)$ by the transport-of-intensity equation for pure phase objects [11, 12]

$$\frac{I^d_\phi(x,y)}{I^0(x,y)} \approx 1 - \frac{d\,\lambda}{2\pi}\,\nabla^2\bar{\varphi}_\phi(x,y), \tag{25}$$

as

$$\bar{g}_\phi(x,y) = -\,\frac{d\,\lambda}{2\pi}\,\nabla^2\bar{\varphi}_\phi(x,y). \tag{26}$$

The function $\bar{g}_\phi(x,y)$ can be interpreted as a projection of an unknown property $g(\underline{x})$. As before the subscript ϕ flags the projection direction. By applying an additional 2dRT to the projection $\bar{g}_\phi(x,y)$, we obtain the 3dRT $\hat{g}_{\phi,\theta}(s)$ of the property g:

$$\hat{g}_{\phi,\theta}(s) = (\mathcal{R}\bar{g}_\phi)(s,\theta) = -\frac{d\,\lambda}{2\pi}(\mathcal{R}(\nabla^2\bar{\varphi}_\phi))(s,\theta). \tag{27}$$

The Radon transform intertwines the two-dimensional Laplacian ∇ and the one-dimensional Laplacian ∂^2/∂_s^2 [13], such that we can relate the 3dRT $\hat{g}_{\phi,\theta}(s)$ of the function $g(\underline{x})$ to the 3dRT $\hat{\varphi}_{\phi,\theta}(s)$ of the phase shift $\varphi(\underline{x})$ by

$$\hat{g}_{\phi,\theta}(s) = -\frac{d\,\lambda}{2\pi}\,\frac{\partial^2}{\partial_s^2}\,(\mathcal{R}\bar{\varphi}_\phi)(s,\theta) = -\frac{d\,\lambda}{2\pi}\,\frac{\partial^2}{\partial_s^2}\,\hat{\varphi}_{\phi,\theta}(s). \tag{28}$$

Thus, we found that for a pure phase object, the 3dRT of the measurable property g is proportional to the second derivative of the 3dRT of the samples phase shift φ. We have seen that for the filtered back projection of 3dRT data the second derivative of the Radon data is back projected (23). Hence, unfiltered back projection of the 3dRT of g yields the 3d structure of the sample's phase shift $\varphi(\underline{x})$.

We have tested this reconstruction scheme on simulated data The phantom consists of 128^3 voxels with 20 randomly distributed homogeneous spheres with 10 pixels radius and a phase shift of $\varphi = -0.02$ rad/voxel. The wavefield behind the object was propagated to a Fresnel number of $F = 1$ using Fresnel propagation [14]. Fig. 8(a) shows the resulting intensity distribution for one projection angle ϕ. For the 3dRT reconstruction a number of 8000 projections was used. A re-projection of the reconstructed phase shift $\varphi(\underline{x})$ is shown in Fig. 8(b).

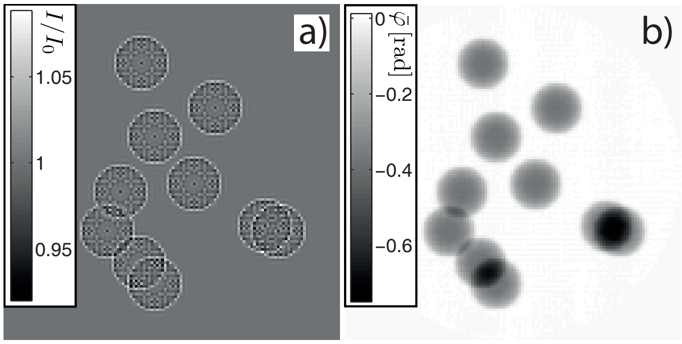

FIG. 8. Pure phase object simulations: (a) intensity distribution for a Fresnel number of $F = 1$. (b) re-projection of the reconstructed phase shift.

VIII. PHASE CONTRAST: EXPERIMENT

For objects with non-negligible absorption (28) is not fulfilled. However, the "*Modified* version of Bronnikov's Algorithm" (MBA) as proposed by A. Groso et. al. [15] can still be successfully used to reconstruct the phase.

Applying this approach to the present 3dRT case, the corresponding 3dRT-MBA reconstructed sinogram of the phase is simply given by

$$\hat{\varphi}^{\mathrm{MBA}}_{\phi,\theta}(s) \simeq -2\pi F \mathcal{F}_s^{-1}\left[\frac{\mathcal{F}_s[\hat{g}_{\phi,\theta}(s)]}{q_s^2+\alpha},\right] \tag{29}$$

where F is the Fresnel number, α is the MBA regularisation parameter, which is increased for higher absorption. $\mathcal{F}_s$ is the 1d Fourier transform with respect to the Radon coordinate s and q_s is the reciprocal coordinate of s. The MBA works well for ideal data (typically for synchrotron results), but fails to yield sharp reconstructions for low coherence laboratory sources. In such cases, an extension of the MBA denoted as "Bronnikov-Aided Correction" (BAC) proposed by Y. De Witte et. al. [16] yields more robust reconstructions of the exit wave. In this algorithm, φ^{MBA} is first computed in an intermediate step, and then used to "undo" the diffraction blurring, yielding an effective object function with contributions from both absorption (low spatial frequencies) and phase (high spatial frequencies). Generalizing this to the 3dRT sinograms, we get

$$\hat{\mu}^{\mathrm{BAC}}_{\phi,\theta}(s) = \hat{\mu}_{\phi,\theta}(s) + \gamma\frac{\partial^2}{\partial s^2}\hat{\varphi}^{\mathrm{MBA}}_{\phi,\theta}(s), \tag{30}$$

where $\hat{\mu}_{\phi,\theta}(s) = \mathcal{R}\left[\ln\left(I^d_\phi/I^0\right)\right]$ is the 3dRT of the logarithm of the normalized measured intensity, $\hat{\mu}^{\mathrm{BAC}}_{\phi,\theta}(s)$ is the 3dRT of the BAC reconstructed absorption and γ is a regularisation parameter.

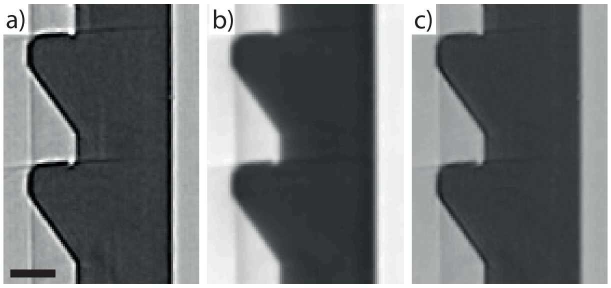

FIG. 9. Phase contrast: Slices through the 3dRT reconstruction of the logarithm of the intensity μ (a), 3dRT-MBA reconstruction of the phase shift φ^{MBA} (b) and 3dRT-BAC reconstruction μ^{BAC} (c). Scale bar: 300 µm.

Fig. 9 shows a slice through the 3dRT reconstructions of the same data set for the measured absorption μ (a), the 3dRT-MBA reconstructed phase shift φ^{MBA} (b) with regularisation parameter $\alpha = 0.2$ and the 3dRT-BAC reconstruction of an effective object function μ^{BAC} (c) with regularisation parameters $\alpha = 0.2$ and $\gamma = 0.5$. The data set was acquired under the same experimental conditions as the match data set (cf. Tab. I). A nylon cable tie was used as sample. The uncorrected absorption (a) shows significant effects of edge enhancement due to propagation effects. The edge enhancement is not visible in the MBA phase reconstruction (b) but sacrifices sharpness. The BAC-reconstructed object function (c) shows significant reduction of edge enhancement while sharpness is maintained.

[1] F. Marone and M. Stampanoni, *J. Synchr. Rad.* **19**, 1029 (2012).
[2] F. Natterer, *The mathematics of computerized tomography* (SIAM, Philadelphia, 2001).
[3] A. G. Ramm and A. I. Katsevich, *The Radon Transform and Local Tomography* (CRC Press, Boca Raton, 1996).

[4] E. B. Saff and A. B. J. Kuijlaars, *Math. Intell.* **19**, 5 (1997).

[5] E. A. Rakhmanov, E .B. Saff, and Y. M. Zhou, *Math. Res. Lett.***1**, 647 (1994).

[6] T. Buzug, *Computed Tomography : From Photon Statistics to Modern Cone-Beam CT* (Springer-Verlag, Berlin Heidelberg, 2008).

[7] An illustrative explanation for this hexagonal tiling is, that the equidistant distribution of N_p points on the unit sphere is a best-packing problem and best packing is usually given by hexagonal assembly. For a detailed explanation see [4].

[8] U. Lundström, D. H. Larsson, A. Burvall, P. A, C Takman, L. Scott, H. Brismar, and H. M. Hertz, *Phys. Med. Biol.* **57**, 2603 (2012).

[9] A. Bronnikov, *Opt. Commun.* **171**, 2394 (1999).

[10] A. Bronnikov, *J. Opt. Soc. Am. A* **19**, 472 (2002).

[11] M. R. Teague, *J. Opt. Soc. Am.* **73**, 1434 (1983).

[12] T. E. Gureyev, C. Raven, A. Snigirev, I. Snigireva, and S. W. Wilkins, *J. Phys. D: Appl. Phys.* **32**, 563 (1999).

[13] A. Markoe, *Analytic Tomography* (Cambridge University Press, Cambridge, 2014), p. 262 f.

[14] D. M. Paganin, *Coherent X-ray Optics* (Oxford University Press, Oxford, 2006).

[15] A. Groso, R. Abela, M. Stampanoni, *Opt.Express* **14**, 8103 (2006).

[16] Y.D. Witte, M. Boone, J. Vlassenbroeck, M. Dierick, and L.V. Hoorebeke *J. Opt. Soc. Am. A* **26**, 890 (2009).